CRYSTAL GROWTH & DESIGN

pubs.acs.org/crystal

Article

Strongly Enhanced Growth of High-Temperature Superconducting Films on an Advanced Metallic Template

Mukarram Z. Khan,* Elmeri Rivasto,* Hannes Rijckaert, Yue Zhao, Maciej O. Liedke, Maik Butterling, Andreas Wagner, Isabel Van Driessche, Hannu Huhtinen, and Petriina Paturi

Cite This: *Cryst. Growth Des.* 2022, 22, 2097−2104

Read Online

ACCESS | Metrics & More | Article Recommendations | Supporting Information

ABSTRACT: We demonstrate a straightforward and easily applied technique for growing $BaZrO_3$ doped $YBa_2Cu_3O_{6+x}$ films of highly improved quality on a commercially used buffered metallic template by pulsed laser deposition. Our method relies on reducing the grain size of the target material, which completely prevents the transfer of the harmful grain boundaries or weak links from the substrate through the buffer layers on the deposited film. We have also observed a great improvement in the self-assembly of $BaZrO_3$ dopants, and the critical current density is increased in the high temperature range up to 40%. As an extra benefit, our method allows us to increasing the growth rate of the film by 25%. We have discussed the results comprehensively and provided quantitative insight into the underlying mechanisms. The presented technique can be considered a groundbreaking advancement for the vastly growing coated conductor industry.

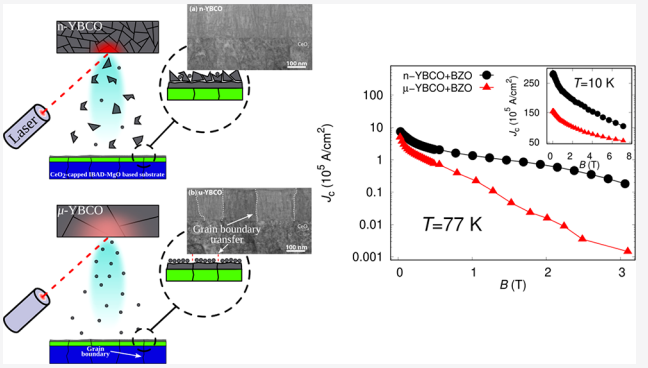

INTRODUCTION

The high-temperature superconductors (HTS) have been of interest for various applications ever since their discovery due to the possibility of dissipation of free power transmission at practically accessible temperatures. These applications range from simple power transmission lines to state-of-the-art magnets used in fusion reactors. The exploitation of HTS materials has been limited due to their fragile ceramic structure which complicates the production of wires from them. The usability of HTS materials in various applications depends fully on the possibility to reliably grow them on buffered metallic templates enabling the production of flexible HTS cables for practical usage.[1,2] A quality film growth on these templates requires good texturization and chemical stability of the substrate surface.[3] In the field of coated conductors, there are two distinct commonly used methods to achieve these requirements. The first method is to deformation-texturize the metal surface by the rolling assisted biaxially textured substrate approach (RABiTS), where one uses the standard thermomechanical processing in order to obtain smooth biaxially oriented substrates.[4,5] The introduction of various buffer layers is further required for achieving the well structured surface with sufficient stability. Another possibility is to texturize the buffer layer structure during deposition via the ion-beam assisted deposition method (IBAD).[6]

A commonly used deposition method of the superconducting thin film on top of the aforementioned substrates among the coated conductor industry is pulsed laser deposition (PLD), which is actively developed to provide better film growth and to be more cost-effective.[2,7−12] The PLD is an attractive growth method of HTS films, since it effectively allows the addition of dopants within the YBCO matrix.[2,13] These dopants are extremely important, especially for applications that work under high magnetic fields, since they act as pinning centers eliminating the dissipation caused by the movement of the field induced vortices. A huge leap in improving the superconducting critical current at high magnetic fields was the discovery of dopants that self-assemble themselves during the PLD process as YBCO *c*-axis oriented nanorods.[14] Among a wide range of discovered self-assembled dopants, perhaps the most famous one is $BaZrO_3$ (BZO), which we have also used in this work.

Until now, mainly $YBa_2Cu_3O_{6+x}$ (YBCO) and $GdBa_2Cu_3O_{6+x}$ (GdBCO) has managed to grow on these buffered metallic templates utilizing PLD for the large-scale coated conductor manufacturing.[15] However, these nonsingle crystalline templates are extremely harsh growth environments for the films to be deposited due to the presence of the great number of grain boundaries, which are usually transferred on the film deposited on the top of it.[16−20] This grain boundary transfer significantly diminishes the benefits of the HTS materials, such as liquid

Received: September 23, 2021
Revised: March 9, 2022
Published: March 23, 2022

https://doi.org/10.1021/acs.cgd.1c01101
Cryst. Growth Des. 2022, 22, 2097−2104

nitrogen cooling, as they limit the superconducting critial current more substantially in the high temperature range. The critical current, determined by the grain boundaries, has been observed to decrease linearly in zero field as the temperature is increased according to the superconductor−insulator−superconductor (SIS) model.[21−23] More unfortunately, under applied magnetic fields the critical current is suppressed exponentially as a function of temperature,[21] and in some cases the grain boundaries can even become weak links blocking the applied current completely.[24,25]

In this work, we present a new simple and easily accessible method of depositing BZO doped YBCO films on advanced metallic template with IBAD-MgO based buffer layers that almost completely prevents the substrate−film grain boundary transfer. Amazingly, our method also provides a major improvement to the formation of BZO nanorods within the YBCO lattice resulting in 40% increased critical current in the high temperature range and allows 25% faster deposition rate of the film. The presented method is based on increasing the size of the particles emitted from the PLD target by reducing the target material grain size down to nanoscale via sol−gel synthesis.[26,27] The details of the target preparation and the PLD process are presented in the Supporting Information (SI). The advanced metallic template with IBAD-MgO based buffer layers used in this work is presented in Figure 1, and the details of the fabrication process are given in ref 28.

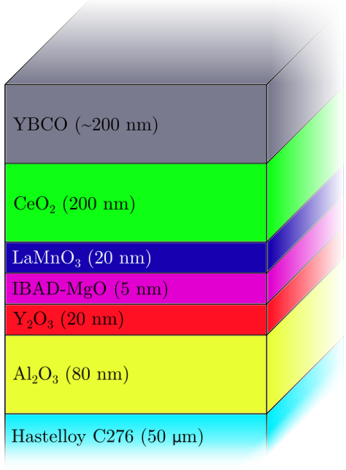

Figure 1. Schematic illustration of the buffer layer structure of the metallic template on top of which the YBCO film has been grown.

The reader should note that the absolute values of J_c presented in this work are not comparable to the values presented in other associated publications, such as in refs 29,30 where higher values of J_c are reported. This is due to the following reasons. First, the magnetically measured J_c's have been proven to result in lower values when compared with the resistively measured ones typically used in the works that report high J_c. This is because the resistive measurements of the critical electric field, that determines the J_c, are substantially less sensitive when compared with the magnetic measurements.[31] Second, it is extremely difficult to compare the resistively measured absolute J_c values between different publicatitons, as there are several factors that can create significant differences between the obtained J_c's, such as film thickness and sample patterning. For example, the films resistively measured in this work were patterned using a wet-chemical etching technique. In this process, our films are exposed to several chemicals and water, which can have a deteriorating effect on superconducting properties. Moreover, we have used a stripe width of only 50 μm for which our measurements are more affected by possible grain boundaries and other lattice defects, as the current is less likely to circulate around them. Thus, in general, the absolute values of J_c should only be compared when the effect of external parameters can be reliably eliminated. In this work, great attention has been put into preparing and measuring the n- and μ-films exactly the same way, in order to exclude all the possible external parameters that may affect the results and focus on studying the fundamental differences in the growth mechanisms between these films.

RESULTS AND DISCUSSION

Grain Boundary Transfer. The commonly used YBCO targets for the PLD process are produced by the solid-state ceramic method resulting into a pellet formed by micrometer-sized grains (μ-YBCO).[32] However, the production of a YBCO target with greatly reduced grain size (n-YBCO) is also possible by utilizing the citric acid combustion variant of the sol−gel method, the details of which can be found in our previous works.[26,27] The morphological properties of both intrinsic n-YBCO and μ-YBCO are presented and extensively studied in ref 33 where the average grain size for n-YBCO was estimated to be from a few tens to a few hundred nanometers, while for μ-YBCO, it was estimated to be several microns. That is, the grain sizes between the n- and μ-YBCO targets differ by 2 orders of magnitude.

In this work, films were grown using the aforementioned n-YBCO and μ-YBCO targets doped with 4% BZO on the nonsingle-crystalline buffered CeO_2-capped IBAD-MgO-based metallic template presented in Figure 1. The microstructures of the films were studied in detail with bright field scanning transmission electron microscopy (BF-STEM) and variable energy positron annihilation lifetime spectroscopy (VE-PALS) which provide detailed local and average global information about the microstructures of the samples, respectively. Further details about the measurement techniques are presented in Supporting Information (SI).

The cross-sectional BF-STEM images of the films deposited from the n-YBCO target (n-film) and the μ-YBCO target (μ-film) are presented in Figure 2a,b, respectively. The grain boundary transfer from the substrate to the films is clearly observed for the μ-film as expected. Surprisingly, in the case of the n-film the grain boundary transfer seems to be completely absent. The absence of grain boundary transfer is further illustrated in close-up BF-STEM images of the substrate−film interface presented in Figure 2c,d, where the substrate grain boundaries are located in the middle of the images. In the case of n-YBCO, the grain boundary is not visible in the deposited film shown above, while for μ-YBCO the grain boundary transfer from substrate to film can be clearly observed. Moreover, the BF-STEM images of the n-film reveal larger natural growth defects, in particular, stacking faults and threading dislocations, when compared with the μ-film.

In order to further confirm that the grain boundary transfer in the n-films is immensely reduced, we have measured the volumetric positron (e^+) lifetimes (τ_i) and annihilation intensities (I_i) as a function of implantation energy as presented in Figure 3. The positron implantation energy is proportional to the average distance that the positron can penetrate the sample. If an implanted positron happens to end up inside a void with reduced electron density, such as a lattice defect, the annihilation

https://doi.org/10.1021/acs.cgd.1c01101
Cryst. Growth Des. 2022, 22, 2097−2104

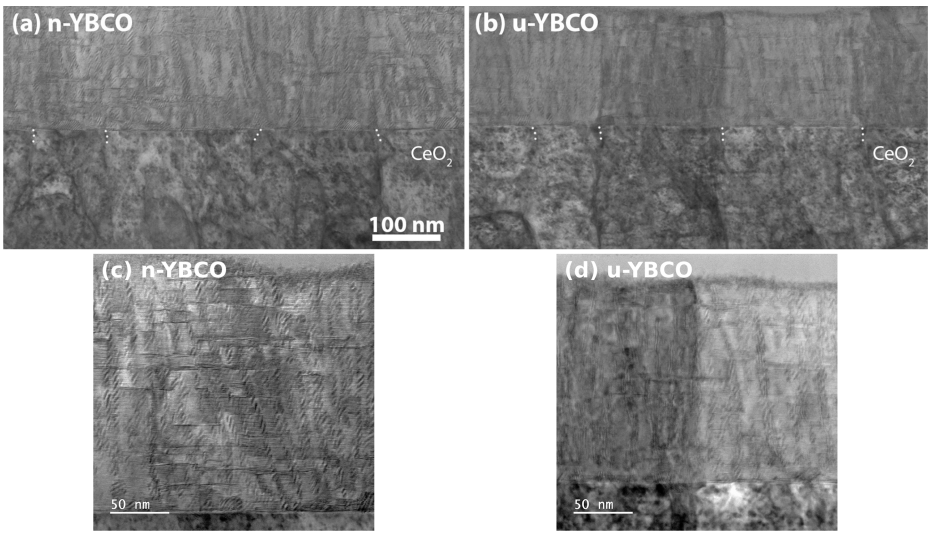

Figure 2. BF-STEM images of (a) n-film and (b) μ-film. The white dotted lines indicate grain boundaries in the metallic template. (c) Close-up image of the n-film at the substrate−film interface with substrate grain boundary in the middle. The grain cannot be observed to transfer to the film. (d) Close-up image of the μ-film at the substrate−film interface with substrate grain boundary in the middle. The grain boundary is clearly transferred to the film above.

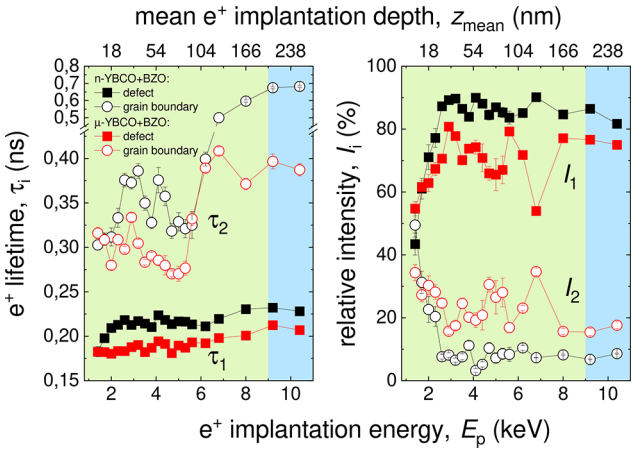

Figure 3. VEPALS analysis of positron lifetimes as a function of positron implantation energy and mean positron implantation depth for both BZO doped n- and μ-YBCO films. The film and substrate regions of both the samples as marked by green and blue colors, respectively. Positron lifetimes components: τ_1 and τ_2 represent annihilation at small vacancies and their agglomerations at grain boundaries, respectively. The relative intensities I_1 and I_2 are related to respective defect densities. The raise of lifetimes for $E_p > 6$ keV is a consequence of the signal superposition with the oxide buffer layer, slightly averaging the both lifetime contributions. The deeper positrons are implanted the larger the fraction of them are annihilated with the buffer due to increasing positron implantation distribution.

of the positron is delayed on a time scale of ~0.1−0.5 ns. This time scale can be further divided into characteristic times representing specific defect types scaling with the available open volume. By measuring the positron annihilation lifetimes, one is then able to probe the presence and size of different types of lattice defects ranging from single vacancies to larger voids in the whole sample.[34,35]

The measured e^+ lifetimes revealed two major characteristic times. The measured short positron lifetime τ_1 is in the range typical for single cation vacancy or neutral oxygen vacancy and their complexes,[36−39] while longer lifetime τ_2 represents vacancy complexes (agglomerations of multiple vacancies) situated at grain boundaries. As seen in Figure 3, the n-film has longer positron lifetimes for both the natural growth defects as well as grain boundaries. This is in line with the BF-STEM measurements which indicated the presence of defects with increased size in the n-film. Dislocations without attached vacancies are usually shallow positron traps (weakly bounding positrons), becoming much stronger as a complex with a vacancy.[40] The increased number of threading dislocations in the n-film observed by BF-STEM could be related with a raise of vacancy concentration, considering larger measured τ_1 for the n-film. Figure 3 also presents the relative intensities of both lifetime components which, very intuitively, are related to the numbers of the associated defects. The relative intensity for grain boundaries is clearly higher for μ-YBCO across the overall film thickness, which is direct evidence that the grain boundary transfer is globally strongly reduced in the n-film.

Although the relative intensity does not drop to zero, still the substantial reduction of the grain boundary density is expected. Considering the fact that the positron trapping yield is proportional to the defect size,[34] the increase of τ_2 should lead to a raise of relative intensity I_2. On the contrary, I_2 is reduced, predicting a large decrease of the respective annihilation state, here the grain boundary. In addition, the scattering of I_2 across the film thickness is larger in the case of μ-films, which is likely related to the defects nanostructure generated by smaller and more abundant BZO nanorods, in contrast to the n-films with the rods extending nearly through the whole film thickness. The above considerations are nicely visualized in Figure 7.

In order to comprehensively understand why the grain boundary transfer is absent when the film is deposited from the n-YBCO target we propose a simple one-dimensional model where the grain boundary of the substrate is assumed to act as a Gaussian potential hill $U(x) = \exp(-x^2/2\sigma^2)$ experienced by the particle emitted from the target as schematically illustrated in Figure 4a. The full width at half-maximum (fwhm) of the potential hill to which, for simplicity, we refer as the Gaussian root-mean-square width σ, is assumed to be proportional to the width of the grain boundary w by relation $\sigma = w/2$. The

https://doi.org/10.1021/acs.cgd.1c01101
Cryst. Growth Des. 2022, 22, 2097−2104

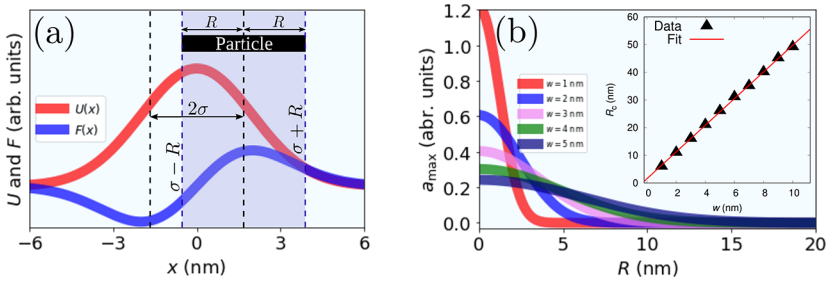

Figure 4. (a) Gaussian potential $U(x)$ centered at $x = 0$ and the force $F(x) = \partial_x U(x)$. The black dashed lines present the σ of the Gaussian potential at which the center of the mass of the particle of radius R (indicated in the figure) is located. The blue dashed lines delimit the region of integration. (b) Main: The maximum acceleration experienced by a nucleation particle size of radius R in the vicinity of a grain boundary of width w. Inset: Calculated critical particle radii, above which the $a_{max} < 10^{-5}$, as a function of grain boundary width.

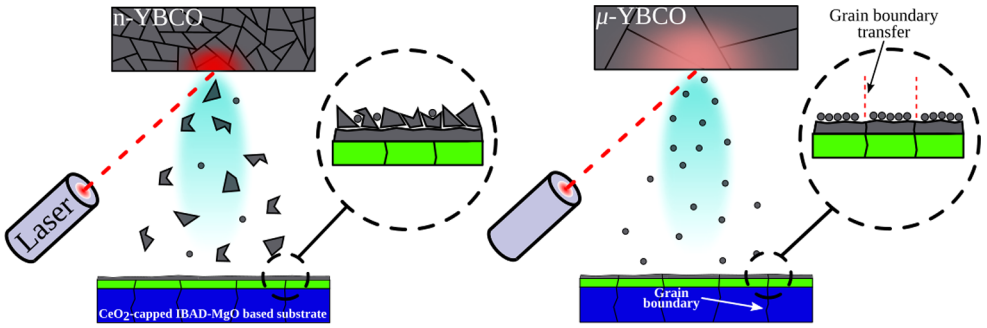

Figure 5. Schematic illustration of the PLD process for n- and μ-grain-sized YBCO targets on a non-single-crystalline buffered CeO_2-capped IBAD-MgO-based metallic template. The ablated particles from the n-target are considered to be clusters of atoms with the size scale being on the order of ~10 nm, while the particles emitted from the μ-target are considered as single atoms.

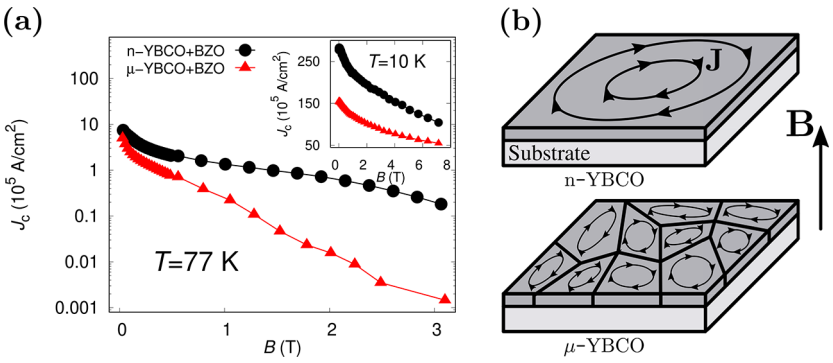

Figure 6. (a) Magnetically measured J_c at 10 and 77 K as a function of the magnetic field for n- and μ-films. (b) Schematic illustration of the magnetic field induced shielding current circulation in the n- and μ-films.

maximum force experienced by a particle is obtained when the center of mass of the particle is located at a point where $\partial_x{}^2 U(x) = 0$, that is at $x = \pm\sigma$. We consider the one-dimensional particle as a homogeneous rigid body of length $2R$ in order to express the mass of the particle (m) with a simple relation $m \sim R$. With the aforementioned relations, the maximum acceleration of the rigid body particle can be calculated by using the simple Newtonian dynamics formula $a(x) = \partial_x U(x)/m$ obtaining

$$a_{max}(R, \sigma) \sim \frac{1}{R\sigma^2} \int_{\sigma-R}^{\sigma+R} x\, e^{-x^2/2\sigma^2}\, dx \qquad (1)$$

where $\sigma = w/2$. The reasoning of eq 1 is illustrated in Figure 4, while a detailed derivation of eq 1 is presented in the SI. The calculated $a_{max}(R)$ curves for various widths of grain boundaries are presented in the main panel of Figure 4b. In all cases, the a_{max} is readily reduced as the particle size is increased, suggesting that the effect of the grain boundary on the growth of the film is highly reduced by increased particle size. In order to further estimate the effect of a grain boundary of size w to an arbitrary size particle, we have defined the particle critical radius (R_c) as the radius above which $a_{max} < 10^{-5}$. The numerically calculated R_c values as a function of w are presented in the inset of Figure 4b. One can observe a clear linear dependence of $R_c(w) = 4.59w + 2.7$ nm. Typical length scale of the grain boundaries is around 2 nm, suggesting that the particle radii emitted from the target would have to be increased only up to 12 nm in order to prevent the grain boundary transfer.

As explained in our previous work,[33] a larger grain size of the μ-YBCO target enhances heat diffusion from the laser pulse to the interior of the target as the grain size is inversely proportional to the number of oxygen-filled grain boundaries that act as thermal insulators. This limits the energy density on the surface of the target enabling the emission of mainly single atoms of unit cells that interact strongly with the grain boundaries of the

https://doi.org/10.1021/acs.cgd.1c01101
Cryst. Growth Des. 2022, 22, 2097−2104

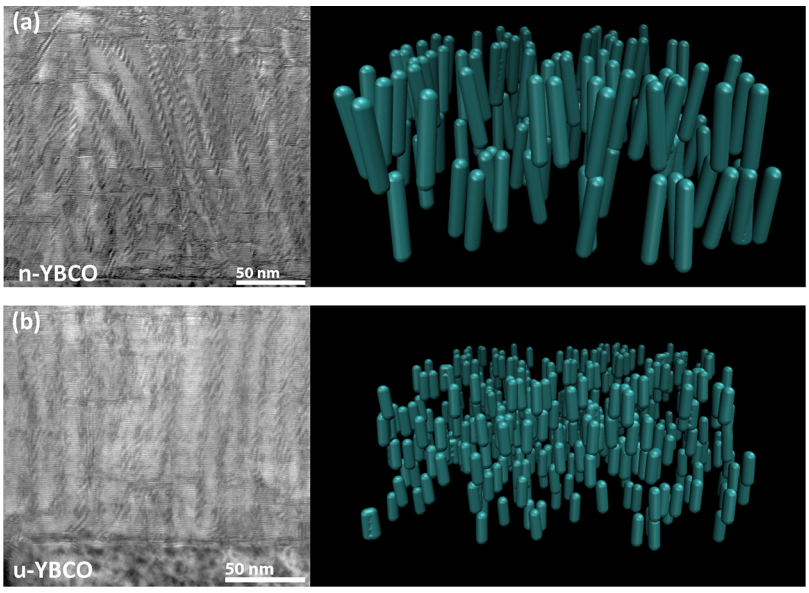

Figure 7. BF-STEM images and 3D schematic illustrations of the observed distributions of the BZO nanorods for (a) n-film and (b) μ-film based on parameters presented in Table 1 obtained from several different BF-STEM images.

substrate, according to the arguments presented above. In the case of the n-YBCO target, that is filled with the insulating grain boundaries, one can achieve greatly enhanced energy density on the surface of the target allowing the emission of large clusters for which the grain boundary interaction is highly reduced. The 12 nm critical particle radius proposed by the introduced theory is certainly in the plausible range to be emitted from the n-YBCO target. The fact that the n-film was observed to have larger and greater number of natural growth defects is also in line with the proposed theory, as the increased size of emitted particles is associated with highly increased formation of individual growth islands on the substrate, as suggested by molecular dynamic simulations presented in ref 33. As more matter is transferred from the n-target to the substrate per pulse, this intuitively results in a faster growth rate manifested as the n-film being 40 nm thicker when compared with the μ-film grown with the same number of pulses. The differences of the proposed PLD processes using different grain sized targets are illustrated in Figure 5.

Effect of Grain Boundaries. The deteriorating effect of the grain boundaries on superconductivity in the high temperature range is dramatically manifested as the critical current density (J_c) was determined by measuring the magnetic hysteresis loop of the n- and μ-films and then calculating the J_c from the openings of the measured loops as suggested by the Bean model.[41] The magnetically measured J_c's as functions of applied magnetic fields at 10 and 77 K are presented in Figure 6a. At 10 K, the n-film is observed to have on average 1.7 times higher J_c when compared with the μ-film. However, at 77 K the J_c of the n-film is observed to become over 100 times greater when compared with the μ-film as the field is increased over 2 T. This overwhelming difference of J_c between the n- and the μ-film demonstrates the effectiveness of the grain boundaries in resisting the passage of Cooper pairs through them, in particular, in the high temperature range as the magnetic field induced weak eddy currents become unable to pass the numerous grain boundaries in the μ-film. Thus, the different grains in the μ-film act more or less as individual superconducting films as illustrated in Figure 6b, and the J_c calculated by the Bean model gives remarkably lower values for the μ-film. As grain boundaries and weak links can be generally considered as Josephson junctions, the fact that they resist Cooper pair passage more in the high temperature limit can be explained by the quantum mechanical Ambegaokar−Halperin model (SIS-model), according to which the critical current density across the grain boundary has a temperature dependence of $J_c \sim (1 - T/T_c)^n$, where $1 \leqslant n \leqslant 2$ depending on the temperature range and T_c is the critical temperature.[21−23] This suggests that the effective grain size, inside which the magnetic field induced eddy currents circulate, becomes smaller as the temperature is increased, thus resulting in a more substantial difference of magnetically measured J_c's between the films in the high temperature range. The onset T_c values were magnetically measured as 85.5 and 83.5 K for the n-film and the μ-film, respectively, while resistive measurement suggests similar T_c around 90 K for both of the films.

Nanorod Formation and Transport Properties. Another significant difference between the deposited n- and μ-films is the formation of the BZO nanorods as seen in Figure 7a,b and Table 1, that summarizes the parameters obtained from the analyzed BF-STEM images. The effect of the nanorods, when it comes to flux pinning, is highly determined by their fragmentation, as more solid nanorods enable greater critical current densities, in particular, in the high field range, as suggested by experiments and simulations of corresponding systems.[42,43] In the case of n-YBCO, the length of the nanorods varies between 75 and 150 nm, while for the μ-film the length is only 25−45 nm. That is, the

Table 1. Compilation of Microscopic Results Measured by BF-STEM for BZO Doped YBCO Grown by Different Grain Sized Targets

parameter	n-film	μ-film
Film thickness (nm)	200−210	160−170
Stacking fault length (nm)	22.8 ± 8.5	21.9 ± 5.0
Nanorod diameter (nm)	7.8 ± 1.4	6.1 ± 1.0
Nanorod length (nm)	75−150	25−45
Nanorod spacing (nm)	12.3 ± 3.6	10.3 ± 2.8
Nanorod splay (°)	15.2 ± 3.3	7.5 ± 1.7

https://doi.org/10.1021/acs.cgd.1c01101
Cryst. Growth Des. 2022, 22, 2097−2104

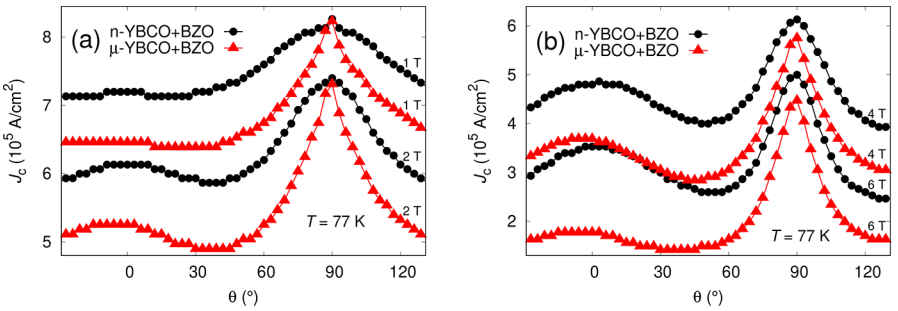

Figure 8. Angular dependence of the J_c in (a) low magnetic field and (b) high magnetic field ranges. The 0° angle is along the YBCO *c*-axis.

nanorods in the n-film are on average over 3 times longer suggesting superior transport properties of the n-film under high magnetic fields when compared to the μ-film. Interestingly, the nanorods are also splayed twice as much in the n-film when compared with the μ-film. Such a huge difference in the length of the nanorods was also observed in our previous work,[42] where n- and μ-films were grown on a single crystalline substrate. We conclude that the improved formation of the nanorods is directly related to the reduced grain size of the target and is not due to the substrate. The n-film can also be observed to grow on average 40 nm thicker when compared with the μ-film with the same number of pulses in the PLD process. This is most likely related to the larger particle sizes emitted from the n-YBCO target, as discussed previously.[42,44] The almost 25% faster film growth with highly improved film quality should attract the coated conductor industry into using the nanosized YBCO targets.

In order to study whether the absence of grain boundaries and the improved nanorod growth actually make the transport properties on the n-film superior when compared with the μ-film; the magnetic field angle (θ) dependence of the J_c was resistively measured in a wide field range. The $J_c(\theta)$ curves measured at high temperature are presented in Figure 8. The shapes of the $J_c(\theta)$ are very similar between the n- and μ-films and above 1 T; a clear improvement of J_c can be seen around θ = 0 (*c*-peak), which is the fingerprint of YBCO with *c*-axis oriented BZO nanorods. The absolute values of J_c show an impressive 40% improvement of J_c in the n-film along the YBCO *c*-axis when compared with the μ-film. Interestingly, the J_c along the YBCO *ab*-axis is approximately the same for both films, suggesting that the improved J_c at $\theta < 90°$ is in particular due to increased vortex pinning performance of the n-film.

Finally, in order to study how much the nanorods control the anisotropy of the critical current ($J_c(\theta)$), the $J_c(\theta)$ curves were simulated using the molecular dynamics method at 1 T for pinning landscapes resembling the observations of the structures of the BZO nanorods in the BF-STEM images presented in Table 1 for n- and μ-films, respectively. Detailed information about the simulation model used is provided in the SI. The pinning landscapes used for n- and μ-films are illustrated in Figure 7 and the simulated critical current anisotropies are presented in Figure 9. The simulations are in line with the experimental measurements as the *c*-peak is absent for both of the films at 1 T and the difference of the absolute values of J_c for the n- and μ-films is clearly reduced at higher angles. This suggests that the pinscape formed by the BZO nanorods mainly determines the critical current anisotropy of the associated film, despite the substantial differences in the grain boundaries and other defects between the films.

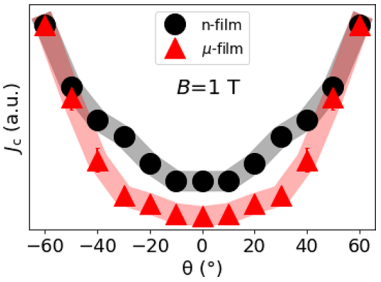

Figure 9. Normalized shapes of the simulated critical current density anisotropies under 1 T applied field considering only the effect of nanorods. The zero angle corresponds to a field parallel to the YBCO *c*-axis.

CONCLUSIONS

We have introduced a new method of using the target with nanosized grains to highly improve the quality of PLD deposited BZO-doped YBCO films on buffered metallic templates via elimination of grain boundaries and improved self-assembly of nanorods. The improved film quality is manifested in particular by the 40% improved J_c along the YBCO *c*-axis. Furthermore, we have provided a widely applicable theory for the grain boundary transfer from substrate to film, which could be of great interest also in research outside the HTS coated conductors. Also, the usage of the target material with nanosized grains in the PLD process may be of great interest in other fields of materials science.

EXPERIMENTAL DETAILS

The n- and μ-grain size targets were synthesized via a citric acid combustion variant of the sol−gel method and solid-state ceramic method, respectively. The films were deposited via PLD at 775 °C with 308 nm laser pulse of 65 mJ at 5 Hz frequency under 0.175 Torr oxygen circulation. The films were given *in situ* post-annealing treatment of 1 atm oxygen for 10 min at 750 °C.

Both magnetic and transport measurements were carried out by the Quantum Design physical property measurement system (PPMS). For transport measurements, 200-μm-wide stripes were patterned on the surface of the film via photolithography and wet chemical etching. The stripes were connected to the PPMS sample holder with a wire bonder using 50 μm wide aluminum wire.

The samples were prepared for the BF-STEM measurements by cutting and milling a cross-sectional lamella via focused ion beam technique. The lamella were extracted using an *in situ* lift-out procedure after which the STEM was carried out with BF detector on operating voltage of 200 kV.

The VEPALS measurements were performed at the monoenergetic positron spectroscopy beamline, which is the end station of the radiation source ELBE at HZDR, Germany.

Further details about sample preparation and measurements are provided in SI.

https://doi.org/10.1021/acs.cgd.1c01101
Cryst. Growth Des. 2022, 22, 2097−2104

■ ASSOCIATED CONTENT

Supporting Information

The Supporting Information is available free of charge at https://pubs.acs.org/doi/10.1021/acs.cgd.1c01101.

Detailed explanations of the following topics: target preparation, PLD process, BF-STEM measurements, VEPALS measurements, magnetic and transport measurements, vortex dynamics simulations, and theory for grain boundary transfer. (PDF)

■ AUTHOR INFORMATION

Corresponding Authors

Mukarram Z. Khan − *Wihuri Physical Laboratory, Department of Physics and Astronomy, University of Turku, 20014 Turku, Finland; University of Turku Graduate School (UTUGS), University of Turku, 20014 Turku, Finland;* Present Address: Bluefors Oy, Helsinki, Finland; orcid.org/0000-0001-6903-2308; Email: mukarram.khan@bluefors.com

Elmeri Rivasto − *Wihuri Physical Laboratory, Department of Physics and Astronomy, University of Turku, 20014 Turku, Finland; University of Turku Graduate School (UTUGS), University of Turku, 20014 Turku, Finland;* orcid.org/0000-0002-1255-0726; Email: elmeri.o.rivasto@utu.fi

Authors

Hannes Rijckaert − *SCRiPTS, Department of Chemistry, Ghent University, 9000 Ghent, Belgium;* orcid.org/0000-0002-6078-2919

Yue Zhao − *School of Electronic Information and Electrical Engineering, Shanghai Jiao Tong University, 200240 Shanghai, People's Republic of China;* orcid.org/0000-0002-7231-2156

Maciej O. Liedke − *Institute of Radiation Physics, Helmholtz-Zentrum Dresden - Rossendorf, 01328 Dresden, Germany*

Maik Butterling − *Institute of Radiation Physics, Helmholtz-Zentrum Dresden - Rossendorf, 01328 Dresden, Germany*

Andreas Wagner − *Institute of Radiation Physics, Helmholtz-Zentrum Dresden - Rossendorf, 01328 Dresden, Germany*

Isabel Van Driessche − *SCRiPTS, Department of Chemistry, Ghent University, 9000 Ghent, Belgium;* orcid.org/0000-0001-5253-3325

Hannu Huhtinen − *Wihuri Physical Laboratory, Department of Physics and Astronomy, University of Turku, 20014 Turku, Finland*

Petriina Paturi − *Wihuri Physical Laboratory, Department of Physics and Astronomy, University of Turku, 20014 Turku, Finland*

Complete contact information is available at: https://pubs.acs.org/10.1021/acs.cgd.1c01101

Author Contributions

M.Z.K. conceived and designed the project. M.Z.K. prepared the samples and performed the magnetic and the transport measurements. E.R. is solely credited for conceiving the mathematical modelings and carrying out simulations. M.Z.K. and E.R. together analyzed the results and wrote the manuscript. Y.Z. provided the metallic template. M.O.L., M.B., and A.W. conducted the VEPAS measurements and analyzed their results. H.R. performed BF-STEM measurements and did the analysis together with I.V.D. H.H. and P.P. supervised the project. All the authors reviewed and commented on the manuscript. M.Z.K. and E.R. contributed equally.

Notes

The authors declare no competing financial interest.

■ ACKNOWLEDGMENTS

The Jenny and Antti Wihuri Foundation, Finland, is acknowledged for financial support. M.Z.K. and E.R. are grateful to University of Turku Graduate School (UTUGS) for providing general resources. M.Z.K. also thanks the University of Turku Foundation for financial support. H.R. acknowledges support and funding as postdoctoral fellow fundamental research of the Research Foundation - Flanders (FWO) under grant number 1273621N. We would like to thank Ahmed G. Attallah and Eric Hirschmann from Helmholtz-Zentrum Dresden-Rossendorf for assistance. This work was partially supported by the Impulse und Networking fund of the Helmholtz Association (FKZ VH-VI-442 Memriox) and the Helmholtz Energy Materials Characterization Platform (03ET7015). The computer resources of the Finnish IT Center for Science (CSC) and the FGCI project (Finland) are also acknowledged.

■ REFERENCES

(1) Selvamanickam, V.; Hazelton, D.; Motowidlo, L.; Krahula, F.; Hoehn, J.; Walker, M.; Haldar, P. High-temperature superconductors for electric power and high-energy physics. *Journal of Minerals, Metals and Materials Society* **1998**, *50*, 27−30.

(2) MacManus-Driscoll, J. L.; Wimbush, S. C. Processing and application of high-temperature superconducting coated conductors. *Nature Reviews Materials* **2021**, *6*, 587.

(3) Obradors, X.; Puig, T. Coated conductors for power applications: materials challenges. *Supercond. Sci. Technol.* **2014**, *27*, 044003.

(4) Goyal, A.; Norton, D.; Christen, D. a.; Specht, E.; Paranthaman, M.; Kroeger, D.; Budai, J.; He, Q.; List, F.; Feenstra, R.; et al. Epitaxial superconductors on rolling-assisted biaxially-textured substrates (RABiTS): A route towards high critical current density wire. *Applied superconductivity* **1996**, *4*, 403−427.

(5) Goyal, A.; Lee, D.; List, F.; Specht, E.; Feenstra, R.; Paranthaman, M.; Cui, X.; Lu, S.; Martin, P.; Kroeger, D.; et al. Recent progress in the fabrication of high-J_c tapes by epitaxial deposition of YBCO on RABiTS. *Physica C: Superconductivity* **2001**, *357*, 903−913.

(6) Iijima, Y.; Kakimoto, K.; Kimura, M.; Takeda, K.; Saitoh, T. Reel to reel continuous formation of Y-123 coated conductors by IBAD and PLD method. *IEEE transactions on applied superconductivity* **2001**, *11*, 2816−2821.

(7) Wu, Y.; Jiang, G.; Zhu, J.; Wu, D.; Quan, X.; Shi, J.; Suo, H.; Zhao, Y. Ultra-fast growth (up to 100 nm s-1) of heavily doped $EuBa_2Cu_3O_7$ film with highly aligned $BaHfO_3$ nanocolumn structure. *Supercond. Sci. Technol.* **2021**, *34*, 05LT01.

(8) Wu, Y.; Zhao, Y.; Han, X.; Jiang, G.; Shi, J.; Liu, P.; Khan, M. Z.; Huhtinen, H.; Zhu, J.; Jin, Z.; Yamada, Y. Ultra-fast growth of cuprate superconducting films: dual-phase liquid assisted epitaxy and strong flux pinning. *Materials Today Physics* **2021**, *18*, 100400.

(9) Lee, S.; Petrykin, V.; Molodyk, A.; Samoilenkov, S.; Kaul, A.; Vavilov, A.; Vysotsky, V.; Fetisov, S. Development and production of second generation high T_c tapes at SuperOx and first tests of model cables. *Supercond. Sci. Technol.* **2014**, *27*, 044022.

(10) Lao, M; Willa, R; Meledin, A; Rijckaert, H; Chepikov, V; Lee, S; Petrykin, V; Van Driessche, I; Molodyk, A; Holzapfel, B; Hanisch, J In-field performance and flux pinning mechanism of pulsed laser deposition grown $BaSnO_3/GdBa_2Cu_3O_{7-\delta}$ nanocomposite coated conductors by SuperOx. *Supercond. Sci. Technol.* **2019**, *32*, 094003.

(11) Fujita, S.; Muto, S.; Hirata, W.; Yoshida, T.; Kakimoto, K.; Iijima, Y.; Daibo, M.; Kiss, T.; Okada, T.; Awaji, S. Flux-Pinning Properties of $BaHfO_3$-Doped EuBCO-Coated Conductors Fabricated by Hot-Wall PLD. *IEEE Transactions on Applied Superconductivity* **2019**, *29*, 1−5.

(12) Fujita, S.; Muto, S.; Iijima, Y.; Daibo, M.; Okada, T.; Awaji, S. Mechanical Properties of $BaHfO_3$-Doped EuBCO Coated Conductors Fabricated by Hot-Wall PLD on IBAD Template. *IEEE Transactions on Applied Superconductivity* **2020**, *30*, 1−5.
(13) MacManus-Driscoll, J.; Foltyn, S.; Jia, Q.; Wang, H.; Serquis, A.; Civale, L.; Maiorov, B.; Hawley, M.; Maley, M.; Peterson, D. Strongly enhanced current densities in superconducting coated conductors of $YBa_2Cu_3O_7 - x$+$BaZrO_3$. *Nature materials* **2004**, *3*, 439−443.
(14) Maiorov, B.; Baily, S.; Zhou, H.; Ugurlu, O.; Kennison, J.; Dowden, P.; Holesinger, T.; Foltyn, S.; Civale, L. Synergetic combination of different types of defect to optimize pinning landscape using $BaZrO_3$-doped $YBa_2Cu_3O_7$. *Nature materials* **2009**, *8*, 398−404.
(15) Yamada, Y.; Ibi, A.; Fukushima, H.; Takahashi, K.; Miyata, S.; Kuriki, R.; Kobayashi, H.; Konishi, M.; Kato, T.; Hirayama, T.; Shiohara, Y. GdBaCuO and YBaCuO Long Coated Conductors by IBAD-PLD Method—Enhancement of Production Speed and Critical Current in a Magnetic Field. *IEEE Transactions on Applied Superconductivity* **2007**, *17*, 3371−3374.
(16) Feldmann, D. M.; Reeves, J. L.; Polyanskii, A.; Kozlowski, G.; Biggers, R. R.; Nekkanti, R. M.; Maartense, I.; Tomsic, M.; Barnes, P.; Oberly, C. E.; et al. Influence of nickel substrate grain structure on $YBa_2Cu_3O_{7-x}$ supercurrent connectivity in deformation-textured coated conductors. *Appl. Phys. Lett.* **2000**, *77*, 2906−2908.
(17) Zhao, Y.; Ma, L.; Wu, W.; Suo, H.-L.; Grivel, J.-C. Study on advanced $Ce_{0.9}La_{0.1}O_2/Gd_2Zr_2O_7$ buffer layers architecture towards all chemical solution processed coated conductors. *Journal of Materials Chemistry A* **2015**, *3*, 13275−13282.
(18) Lao, M.; Hecher, J.; Pahlke, P.; Sieger, M.; Hühne, R.; Eisterer, M. Magnetic granularity in pulsed laser deposited YBCO films on technical templates at 5 K. *Supercond. Sci. Technol.* **2017**, *30*, 104003.
(19) Wang, Y.; Zhou, L.; Li, C.; Yu, Z.; Li, J.; Jin, L.; Wang, P.; Lu, Y. Texture Transfer Mechanism of Buffer Layer in Coated Conductors. *Journal of superconductivity and novel magnetism* **2012**, *25*, 811−816.
(20) Mihalache, V.; Stefan, N.; Enculescu, I.; Mihailescu, I.; Socol, M.; Miroi, M. The influence of the microstructure and morphology of CeO_2 buffer layer on the properties of YBCO films PLD grown on Ni tape. *Journal of Superconductivity and Novel Magnetism* **2014**, *27*, 2475−2485.
(21) Mannhart, J.; Chaudhari, P.; Dimos, D.; Tsuei, C. C.; McGuire, T. R. Critical Currents in [001] Grains and across Their Tilt Boundaries in $YBa_2Cu_3O_7$ Films. *Phys. Rev. Lett.* **1988**, *61*, 2476−2479.
(22) Hilgenkamp, H.; Mannhart, J. Grain boundaries in high-T_c superconductors. *Rev. Mod. Phys.* **2002**, *74*, 485.
(23) Steel, D. G.; Hettinger, J. D.; Yuan, F.; Miller, D. J.; Gray, K. E.; Kang, J. H.; Talvacchio, J. Electrical transport properties of [001] tilt bicrystal grain boundaries in $YBa_2Cu_3O_7$. *Appl. Phys. Lett.* **1996**, *68*, 120−122.
(24) Dimos, D.; Chaudhari, P.; Mannhart, J. Superconducting transport properties of grain boundaries in $YBa_2Cu_3O_7$ bicrystals. *Phys. Rev. B* **1990**, *41*, 4038−4049.
(25) Babcock, S. E. High-Temperature Superconductors from the Grain Boundary Perspective. *MRS Bull.* **1992**, *17*, 20−26.
(26) Raittila, J.; Huhtinen, H.; Paturi, P.; Stepanov, Y. P. Preparation of superconducting $YBa_2Cu_3O_{7-\delta}$ nanopowder by deoxydation in Ar before final oxygenation. *Physica C: Superconductivity* **2002**, *371*, 90−96.
(27) Paturi, P.; Schlesier, K.; Huhtinen, H. Effect of target density on YBCO thin films deposited from nanograined targets. *Physica C: Superconductivity* **2009**, *469*, 839−842.
(28) Zhao, Y.; Zhu, J.-M.; Jiang, G.-Y.; Chen, C.-S.; Wu, W.; Zhang, Z.-W.; Chen, S. K.; Hong, Y. M.; Hong, Z.-Y.; Jin, Z.-J.; Yamada, Y. Progress in fabrication of second generation high temperature superconducting tape at Shanghai Superconductor Technology. *Supercond. Sci. Technol.* **2019**, *32*, 044004.
(29) Suzuki, H.; Yoshida, Y.; Ichino, Y.; Takai, Y.; Awaji, S.; Watanabe, K.; Yoshizumi, M.; Izumi, T.; Shiohara, Y.; Kato, T. J_c anisotropy for magnetic field angle in YBCO coated conductor on IBAD-MgO buffered metal tapes. *Physica C: Superconductivity and its applications* **2010**, *470*, 1384−1387.
(30) Liu, L.; Li, Y.; Wu, X.; Xiao, G.; Xu, D. Development of Long REBCO Coated Conductors by PLD-REBCO/Sputter-CeO 2/IBAD-MgO at SJTU and SSTC. *IEEE Transactions on Applied Superconductivity* **2015**, *25*, 1−4.
(31) Pan, A. V.; Golovchanskiy, I.; Fedoseev, S. Critical current density: Measurements vs. reality. *EPL (Europhysics Letters)* **2013**, *103*, 17006.
(32) Rao, C.; Nagarajan, R.; Vijayaraghaven, R. Synthesis of cuprate superconductors. *Supercond. Sci. Technol.* **1993**, *6*, 1.
(33) Aye, M. M.; Rivasto, E.; Khan, M. Z.; Rijckaert, H.; Salojärvi, E.; Haalisto, C.; Mäkilä, E.; Palonen, H.; Huhtinen, H.; Van Driessche, I.; et al. Control of the nanosized defect network in superconducting thin films by target grain size. *Sci. Rep.* **2021**, *11*, 1−11.
(34) Krause-Rehberg, R.; Leipner, H. S. *Positron annihilation in semiconductors: defect studies*; 1999. DOI: 10.1007/978-3-662-03893-2
(35) Tuomisto, F.; Makkonen, I. Defect identification in semiconductors with positron annihilation: Experiment and theory. *Rev. Mod. Phys.* **2013**, *85*, 1583−1631.
(36) Puska, M. J.; Nieminen, R. M. Theory of positrons in solids and on solid surfaces. *Rev. Mod. Phys.* **1994**, *66*, 841−897.
(37) Jenson, K. O.; Nieminen, R. M.; Puska, M. J. Positron states in $YBa_2Cu_3O_{7-x}$. *J. Phys.: Condens. Matter* **1989**, *1*.
(38) McMullen, T.; Jena, P.; Khanna, S. N.; Li, Y.; Jensen, K. O. Positron trapping at defects in copper oxide superconductors. *Phys. Rev. B* **1991**, *43*, 10422−10430.
(39) Smedskjaer, L.; Veal, B.; Legnini, D.; Paulikas, A.; Nowicki, L. Positron trapping in the superconductor $YBa_2Cu_3O_x$: $Ba_2Cu_3O_x$. *Physica B+C* **1988**, *150*, 56−60.
(40) Assali, S.; Elsayed, M.; Nicolas, J.; Liedke, M. O.; Wagner, A.; Butterling, M.; Krause-Rehberg, R.; Moutanabbir, O. Vacancy complexes in nonequilibrium germanium-tin semiconductors. *Appl. Phys. Lett.* **2019**, *114*, 251907.
(41) Wiesinger, H.; Sauerzopf, F. M.; Weber, H. W. On the calculation of J_c from magnetization measurements on superconductors. *Physica C: Superconductivity* **1992**, *203*, 121−128.
(42) Khan, M. Z.; Rivasto, E.; Tikkanen, J.; Rijckaert, H.; Malmivirta, M.; Liedke, M. O.; Butterling, M.; Wagner, A.; Huhtinen, H.; Van Driessche, I.; et al. Enhanced flux pinning isotropy by tuned nanosized defect network in superconducting $YBa_2Cu_3O_{6+x}$ films. *Sci. Rep.* **2019**, *9*, 1−12.
(43) Rivasto, E.; Khan, M.; Wu, Y.; Zhao, Y.; Chen, C.; Zhu, J.; Huhtinen, H.; Paturi, P. Lattice defect induced nanorod growth in YBCO films deposited on an advanced IBAD-MgO template. *Supercond. Sci. Technol.* **2020**, *33*, 075008.
(44) Aye, M. M.; Rivasto, E.; Khan, M. Z.; Rijckaert, H.; Salojärvi, E.; Haalisto, C.; Mäkilä, E.; Palonen, H.; Huhtinen, H.; Van Driessche, I.; et al. Control of the nanosized defect network in superconducting thin films by target grain size. *Sci. Rep.* **2021**, *11*, 1−11.

https://doi.org/10.1021/acs.cgd.1c01101
Cryst. Growth Des. 2022, 22, 2097−2104